Available online at www.sciencedirect.com
SCIENCE DIRECT®
ELSEVIER
European Journal of Mechanics B/Fluids 23 (2004) 443–460
EUROPEAN JOURNAL OF MECHANICS B/FLUIDS

Instabilities, entrainment and mixing in reacting plumes

K.H. Luo

Department of Engineering, Queen Mary, University of London, London E1 4NS, UK

Received 4 March 2003; received in revised form 7 August 2003; accepted 30 October 2003

Abstract

Dynamics of buoyant reacting flows from rectangular, square and round sources were investigated using Direct Numerical Simulation (DNS). The general three-dimensional time-dependent governing equations for compressible flow and finite-rate Arrhenius chemistry were solved by high-order numerical methods. The study focused on the intricate couplings among instabilities, vortex dynamics, mixing, entrainment, turbulence and combustion through buoyancy. The main dynamic features of buoyant reacting flows, including the puffing phenomenon, were well reproduced. The instability behind puffing was identified as an intrinsic buoyancy instability that arose from density inhomogeneity in the presence of gravity. No external disturbances were required to trigger or sustain the puffing motions, indicating that the buoyancy instability was a global, absolute instability. The base configurations at the inlet had a significant influence on the subsequent vortex dynamics, entrainment, mixing and ultimately the combustion processes. Base configurations with corners, such as squares and rectangles, were associated with higher entrainment rates than those associated with circular jets/plumes, due to the Biot–Savart instability. A new mechanism based on an extension of the Biot–Savart instability clearly elucidated why rectangular jets/plumes entrain more than square ones, despite the fact that both types of configurations have corners. The aspect ratio effects arising from the mechanism could explain the higher level of vorticity and consequently higher entrainment rate along the major axis as compared with those along the minor axis. Axis switching, as may be deduced from the mechanism, was observed in the rectangular case of aspect ratio 3. The main terms in the vorticity transport equations were calculated for this case, and the coupling between vortex dynamics and combustion was scrutinized. The base configurations were seen to trigger different dynamic couplings among instabilities, vortex dynamics, large-scale entrainment, small-scale mixing and combustion. Such couplings were truly two-way, as exemplified by the modification of the energy frequency spectra by chemical heat release.

Keywords: Direct numerical simulation; Instabilities; Vortex dynamics; Entrainment; Mixing; Buoyancy; Turbulence; Combustion

1. Introduction

Understanding, prediction and control of turbulent reacting flows remain a major challenge for this century due to the extremely complicated couplings among flow instabilities, vortex dynamics, turbulence and combustion. Such couplings are especially strong in turbulent non-premixed or diffusion flames, where mixing between the fuel and the oxidizer plays a vital role. Past studies have mostly been concerned with momentum-driven, non-buoyant flames targeted at industrial applications such as compression ignition engines and gas turbines. However, low-speed, buoyancy-driven reacting plumes have important applications too as in space technology, environmental protection and fire safety, etc. The presence of buoyancy effects due to combustion-generated density inhomogeneity greatly complicates the turbulence–combustion interactions. Since such phenomena are inherently unsteady, transient, and have a wide range of time and length scales, few tools are effective

E-mail address: K.H.Luo@qmul.ac.uk (K.H. Luo).

0997-7546/$ – see front matter
doi:10.1016/j.euromechflu.2003.10.008

Nomenclature

Da	Damköhler number
Fr	Froude number defined as $u^{*2}_{\text{ref}}/(g^*_{\text{ref}}L^*_{\text{ref}})$
g_z	gravitational acceleration in z direction ($g_z = -1$)
$\Delta h^\circ_{f,\alpha}$	standard enthalpy of formation
L_i	length of flame base configuration in ith-direction
M_α	chemical symbol for species α
p	pressure
Q_h	a heat release parameter
Q_m	mass flux
Ri	Richardson number defined as $(1-\rho/\rho_a)/\text{Fr}$
Re	Reynolds number
Sc	Schmidt number
St	Strouhal number, non-dimensional frequency defined as $f^*L_{\text{ref}}/U_{\text{ref}}$
t	time
$T,\ T_f$	temperature, flame temperature
$u,\ v,\ w$	velocity components in x, y and z directions, respectively
$\mathbf{V}$	velocity vector
W_α	molecular weight for species α
$x,\ y,\ z$	spatial coordinates
Y_α	mass fraction for species α
Ze	Zeldovich number

Greek

ν_α	stoichiometric coefficient for species α
ξ	mixture fraction defined as $(sY_F - Y_O + 1)/(1+s)$, where $s = \nu_O W_O/\nu_F W_F$
ρ	density
χ	mixture fraction dissipation rate defined as $2\mu/(\text{Re Sc})\nabla\xi\cdot\nabla\xi$
$\lvert\vec{\omega}\rvert$	vorticity magnitude defined as $\sqrt{\omega_x^2+\omega_y^2+\omega_z^2}$
ω_i	vorticity components
$\boldsymbol{\omega}$	vorticity vector
ω_T	reaction rate
$\boldsymbol{\tau}$	viscous stress vector

Superscripts

$*$	dimensional quantity

Subscripts

a	ambient
$F,\ O,\ P$	fuel, oxidizer and product, respectively
i	index for the three Cartesian components $x,\ y$ and z
ref	reference quantity
α	index for chemical species

in unravelling the complicated multi-scale interactions among combustion, buoyancy, instabilities, vortex dynamics and the surroundings. Unsurprisingly, current understanding of the phenomena, especially in the near field, is very poor [1].

There have been theoretical, experimental and numerical studies in the field. Experiments of combustion in low gravity, for example, have been conducted in space laboratories [2]. Whether in space or on the ground, however, experimental studies of flow-combustion interactions, which typically require simultaneous measurement of two or more quantities, are highly difficult and costly. Recent advances in particle image velocimetry (PIV) and planar laser-induced fluorescence (PLIF) have enabled the simultaneous measurement of the two-dimensional (2D) velocity, density and/or temperature field (e.g., [3–5]). However, for truly three-dimensional (3D) fields of turbulent reacting flows, no existing experimental techniques seem to be adequate for providing the temporal and spatial resolution required. In fact, measurement of basic quantities such as the entrainment rate of a

diffusion flame is still subjected to large uncertainties [4]. In the past three decades, various computational techniques have been developed, which, coupled with the availability of ever faster and cheaper computing hardware, have become indispensable tools for research and in some cases for design. In the context of buoyant reacting flows, the Reynolds Averaged Navier–Stokes (RANS) approach has been most widely employed [6]. It is very cost-effective in predicting the average behaviour of reacting plumes away from the source. Close to the source, however, the RANS approach cannot be relied upon to give accurate prediction in the presence of laminar-to-turbulence transition, large-scale entrainment, combustion and strong unsteadiness. In principle, Large Eddy Simulation (LES) can overcome most of these deficiencies, because it accurately resolves the large-scale motions that are responsible for unsteadiness and entrainment. In practice, LES has not been employed extensively for predicting reacting flow, due to the uncertainties in the modelling of combustion and mixing at the subgrid-scale (SGS) level. Nevertheless, some examples of LES studies of buoyant reacting flows have appeared in recent years [7–10]. To avoid the modelling uncertainties, Direct Numerical Simulation (DNS) is desired, which resolves all the scales down to the Kolmogorov micro-scales. Once DNS data is obtained, information can be extracted to enhance fundamental knowledge as well as aid model validation and development. The method is computationally very expensive, which has limited its application. On the other hand, DNS is the only option for many phenomena involving complicated interactions over a range of scales. Moreover, DNS is the only method which provides high-order turbulent statistics such as triple correlations. Therefore, targeted use of DNS for some important but poorly understood phenomena is justified. The buoyant reacting flow in the near field is just one example.

Recently, DNS has seen increased applications for diffusion flames without [11] and with buoyancy [12]. The near-field entrainment rates of reacting plumes from an axisymmetric, square and rectangular sources were very different [13–15], in qualitative but not quantitative agreement with the observations from non-buoyant jets [16]. The presence of solid walls near the source could have a significant effect on entrainment and plume development [17,18]. Such results are of relevance to control of mixing, turbulence and combustion, which is the ultimate goal of the research and can lead to practical exploitation. Moin [19] has promoted DNS as an effective diagnostic tool for forming active and passive turbulence control strategies based on fundamental understanding. However, most studies so far have been related to simulation [20] and control [19] of nonreacting flows. More recently, combustion control using both passive and active means has attracted increasing attention [16,21,22].

In the present study, DNS is employed to study buoyant flame dynamics and entrainment in the near field. The focus is on the effects of the flame base configurations on the complex interactions among fluid dynamics, buoyancy and finite-rate chemistry. The various flow instabilities involved are investigated in detail and their effects on entrainment and mixing are analyzed. The study has relevance to control of combustion where buoyancy effects are important with potential applications for space technology, environment protection and fire safety. The rest of the paper is organized as follows. Section 2 describes details of the numerical procedures used in the DNS and the databases obtained under various conditions. The dynamics and structures of buoyant diffusion flames are presented in Section 3, together with a detailed analysis on the mechanism behind puffing. The Biot–Savart instability is revisited in Section 4 and is used to explain some of the effects of flame base configurations on vortex dynamics, entrainment, mixing and combustion downstream. Section 5 presents a new explanation of the aspect ratio effect, backed by DNS data, and forms a complete description of the flame base configuration effects. The findings from the present study are summarized in Section 6, followed by discussions on unsolved problems. The majority of the mathematical symbols are defined in the Nomenclature whereas some special symbols are defined in the text.

2. DNS databases

A general formulation was used in an in-house DNS code, DSTAR, which solved the full 3D time-dependent compressible Navier–Stokes equations for flow and the species transport equations for finite-rate Arrhenius chemistry [23]. Buoyancy terms $(\rho_a - \rho)g_z/\mathrm{Fr}$ and $(\rho_a - \rho)wg_z/\mathrm{Fr}$ appear in the momentum and the energy equations, respectively, without invoking the Boussinesq assumption [14]. The gravity was aligned in the vertical direction pointing downward so that $g_z = -1$, after normalization. As a result, the full coupling between turbulence and combustion through the fluctuating density and pressure was preserved. Regarding the treatment of chemistry, there has been much controversy about how much detail needs to be incorporated in a DNS. The answer is very much dependent on the physical problem itself. Shu et al. [24] compared a one-step global reaction and a detailed 52-step mechanism in a buoyant methane-air flame, and found the results of flame dynamics and the flickering frequency were essentially the same. In the present study, combustion was represented by a simple generic 1-step, irreversible reaction $\nu_F M_F + \nu_O M_O \to \nu_P M_P$, whose reaction rate was given by the Arrhenius law in the following non-dimensional form

$$\omega_T = \mathrm{Da}\left(\frac{\rho Y_F}{W_F}\right)^{\nu_F}\left(\frac{\rho Y_O}{W_O}\right)^{\nu_O}\exp\left[-\mathrm{Ze}\left(\frac{1}{T}-\frac{1}{T_f}\right)\right], \tag{1}$$

where all the quantities are non-dimensionalized following the convention defined in [14,23]. The corresponding heat release term in the energy equation is $\omega_h = Q_h\omega_T$, where $Q_h = \nu_F W_F \Delta h^\circ_{f,F} + \nu_O W_O \Delta h^\circ_{f,O} - \nu_P W_P \Delta h^\circ_{f,P}$.

Table 1
Simulation parameters

Cases	Q_h	Grid points	Computational box	Sponge layer length
Rectangular I	0	$108 \times 216 \times 288$	$3 \times 6 \times 8$	0.75
Rectangular II	1650	$108 \times 216 \times 288$	$3 \times 6 \times 8$	0.75
Rectangular III	1250	$256 \times 256 \times 384$	$8 \times 8 \times 12$	1.5
Square I	1650	$152 \times 152 \times 304$	$4.25 \times 4.25 \times 8.5$	0.75
Square II	1250	$192 \times 192 \times 288$	$5 \times 5 \times 7.5$	0.75
Round	1250	$192 \times 192 \times 288$	$5 \times 5 \times 7.5$	0.75

The governing equations were solved using a modified 6th-order compact finite difference scheme for spatial discretisation in all three directions and a third-order fully-explicit compact-storage Runge–Kutta scheme for time advancement. The time step is determined by a Courant–Friedrichs–Lewy (CFL) condition for stability, which is dependent on flow convection, diffusion and the chemical reaction, with the chemistry constraint being typically the most stringent. For the present spatial DNS using high-order schemes, the numerical boundary conditions (NBCs) need careful treatment. The characteristic, non-reflecting NBC formulation for compressible, reacting and viscous flows [25] was employed. Close to the outflow boundary, an additional but short sponge layer (see Table 1) was also employed to completely prevent possible spurious wave reflections [17]. The sponge layer essentially enforced a fully developed outflow condition over a short period, instead of imposing it right at the outflow boundary as in many other numerical studies. The data in the sponge layer was not entirely physical, so that it was discarded without any discussion here. For the lateral open boundaries, entrainment was allowed by applying the local one-dimensional inviscid (LODI) relations [25] to the momentum equation, in which the density and temperature were assigned their ambient values.

A series of simulations by DNS were performed of buoyant diffusion flames from round, square and rectangular sources. Table 1 shows the different cases and the corresponding simulation conditions. Other common parameters were $\mathrm{Re} = 1000$, $\mathrm{Sc} = 1$, $\mathrm{Da} = 6$, $\mathrm{Ze} = 12$, $T_f = 6$ and $\mathrm{Fr} = 1.5$. The dynamic viscosity was a function of temperature $\mu = T^{0.76}$. Cases Rectangular I and II were both of an aspect ratio 2, but Rectangular I was a nonreacting counterpart. Case Rectangular III has an aspect ratio 3. To facilitate comparison, the different cases used a common length scale for non-dimensionalization. The diameter of the round source was chosen, which had a non-dimensional value 1. The side lengths of the square and rectangular sources were chosen, so that their areas were equal to that of the round source. The simulations were conducted on a massively parallel computer using 96 to 128 processors. As an example, Case Round used about 10 000 processor-hours.

3. Dynamics of buoyant diffusion flames

In buoyant diffusion flames, there is a dynamic coupling among vortex dynamics, entrainment, mixing, combustion and turbulence through buoyancy. Because of the finite-rate chemistry used, the flame structures are highly sensitive to flow dynamics, which in turn are strongly influenced by combustion-induced buoyancy effects. A typical 3D flame structure and the associated vorticity field are shown in Fig. 2 for case Square II. Near the base, the flame retains its distinctive square shape. "Necking" occurs at about one source width above the base, in agreement with other experiments [26–28] and simulations [29]. Above the neck, the first large vortices form, which is followed by an intermittent flaming zone. Further above, the flame exhibits changing structure and transient dynamic behavior, characteristic of turbulent diffusion flames. Holes appear in the flame structure, which are mainly caused by large-scale vortical motions, although local flame extinction may not be excluded. Note that the iso-surface plots in Fig. 2 show only one value of the reaction rate ω_T and the total vorticity magnitude $|\vec{\omega}| = \sqrt{\omega_x^2 + \omega_y^2 + \omega_z^2}$, which define the dominant square features. In reality, small-scale, almost random motions are present, especially in the far field.

One of the prominent phenomena in buoyant reacting flows is puffing or flame flickering, which exhibits as a quasi-periodic, self-sustained fluctuation, and rollup of large vortices near the base. Much controversy still exists regarding the mechanism behind the phenomenon, although some consensus has appeared in recent years. Buckmaster and Peters [30] proposed that the hydrodynamic Kelvin–Helmholtz instability modified by buoyancy was behind the flame flickering. Ghoniem et al. [29] believed the Rayleigh–Taylor instability also had a contribution. Cetegen and Ahmed [26] found that the puffing frequencies of non-reacting buoyant plumes and reacting plumes had a similar scaling with the source diameter (or the Richardson number after normalization), suggesting that the mechanisms behind must be the same. Others [9,27,31,32] discussed the puffing mechanism in terms of convective and absolute instabilities. Cetegen [27] believed the puffing mechanism was of a convective instability type whereas Maxworthy [32] and Zhou et al. [9] found it to be of an absolute instability type. Katta et al. [33] and Jiang

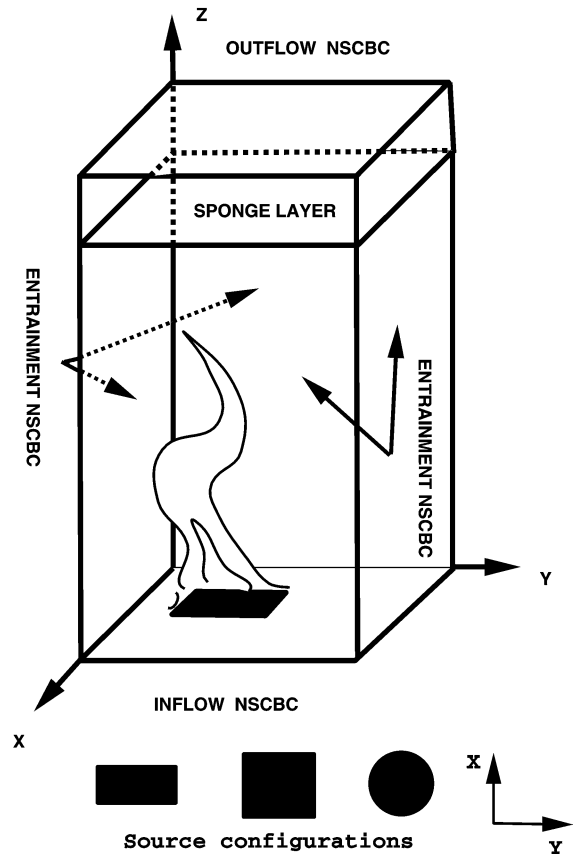

Fig. 1. The computational configurations and boundary conditions.

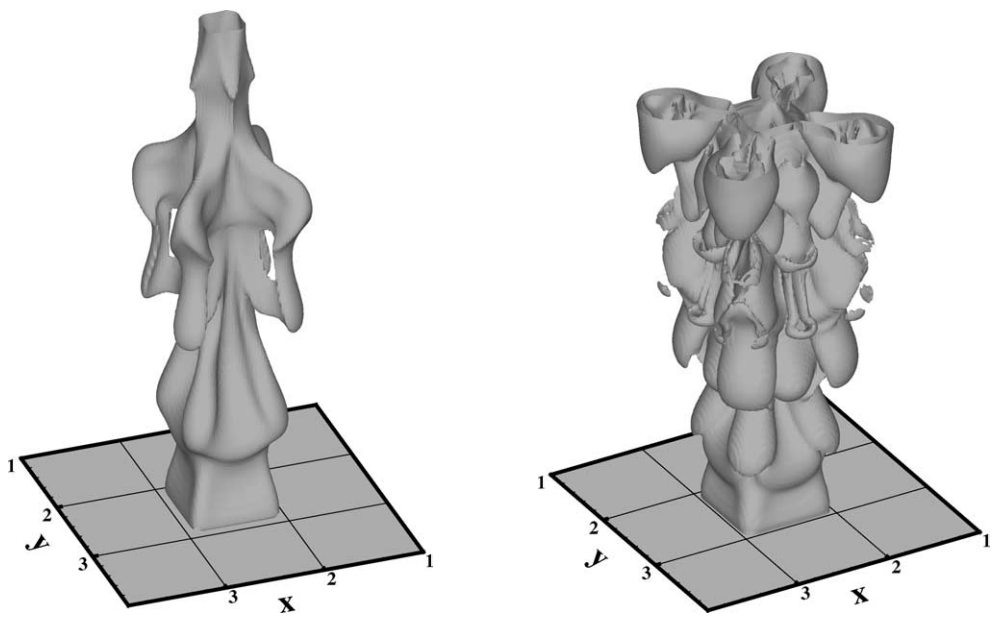

Fig. 2. Reaction rate iso-surface $\omega_T = 0.29\omega_{T,\max}$ (left) and vorticity magnitude iso-surface $|\vec{\omega}| = 0.22|\vec{\omega}|_{\max}$ (right) at $t = 24$ of the buoyant reacting plume from a square source (Square II).

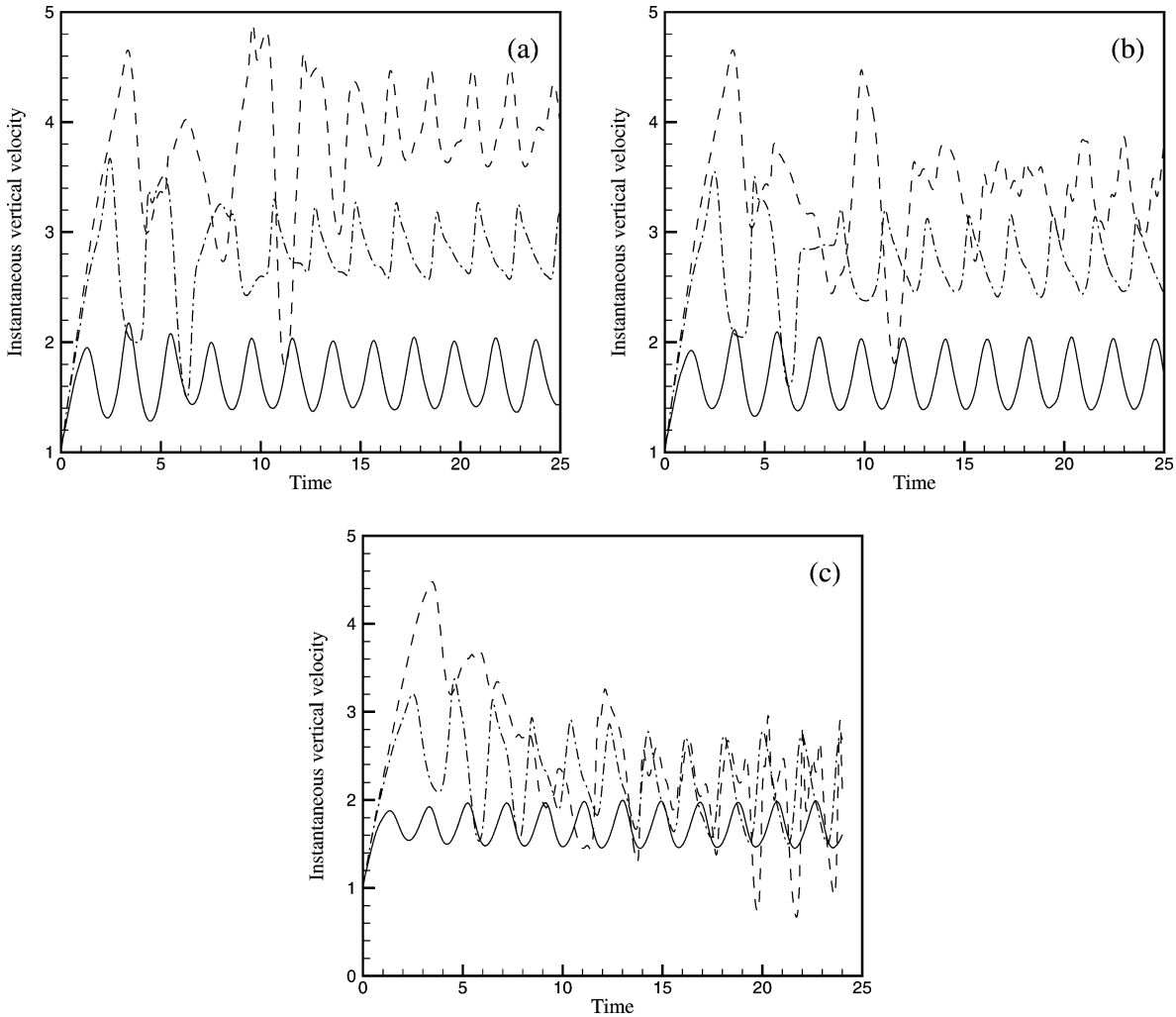

Fig. 3. Time traces of the vertical velocity w at three vertical locations along the centre lines for cases (a) Round; (b) Square II; and (c) Rectangular II (— $z = 1$; –·– $z = 3$; – – – $z = 6$).

and Luo [13] observed in buoyant diffusion flames that the inner, smaller Kelvin–Helmholtz vortices were triggered by small disturbances whereas the buoyancy-driven outer, larger vortices developed without any perturbation.

In the present simulations, laminar non-premixed flame conditions were applied at the inflow, *without* any external perturbations, unlike the non-buoyant jet simulations [34,35] or buoyant plume experiments [27]. The fuel entered vertically into a quiescent oxidizer ambient at an initial temperature ratio 3, similar to the conditions at the inflow used in [29]. Combustion was started by an auto-ignition process facilitated by the hot fuel. The characteristic puffing or flame flickering phenomenon was observed in all buoyant reacting plume cases and in the buoyant thermal plume case (Rectangular I). Fig. 3 shows the time traces of the instantaneous vertical velocity at three heights along the centre lines for cases Round, Square II and Rectangular II. In all cases, the periodic fluctuations are easily identified near the sources. In the downstream, higher frequency fluctuations appear, but the puffing motions are still visible in cases Round and Square II. In the more "turbulent" case of Rectangular II, the puffing frequency is almost invisible at $z = 6$. However, it will be shown in Fig. 5 that the puffing motions have not disappeared and are the most energetic even at that height. These results indicate that the periodic fluctuations initiated from the buoyancy source have spread to the whole flow field. Therefore, the puffing phenomenon is a *global instability* by the definition of Huerre and Monkewitz [36]. Fig. 4 shows the energy frequency spectra of the thermal plume case Rectangular I. Near the source, there is a dominant unsteady mode at the non-dimensional puffing frequency or the Strouhal number of about 0.5. In the downstream, several harmonics of the puffing frequency have also appeared. In the corresponding reacting case Rectangular II shown in Fig. 5, the puffing frequency is also 0.5 at both heights. This value can also be obtained from Fig. 3 by manually

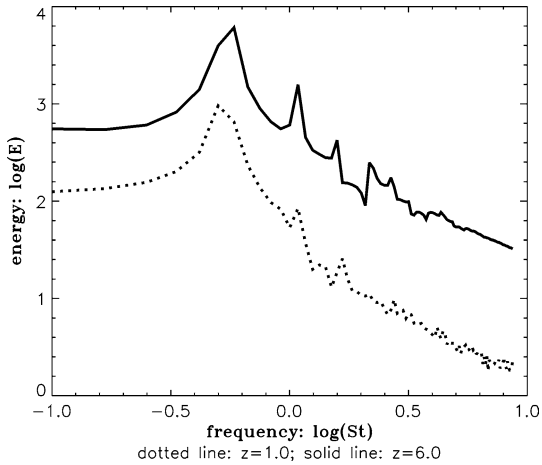

Fig. 4. Energy frequency spectra based on the instantaneous centerline velocity w at two vertical locations in the thermal plume (Rectangular I).

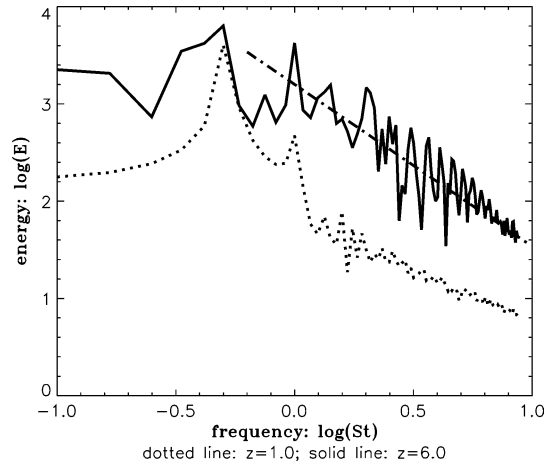

Fig. 5. Energy frequency spectra based on the instantaneous centerline velocity w at two vertical locations in a rectangular reacting plume (Rectangular II), compared with the Kolmogorov $-5/3$ power law.

counting the periods of oscillations within certain simulation time. The other puffing frequencies are 0.50 for case Square I, 0.47 for case Square II and 0.49 for case Round. For buoyant round plumes, Cetegen [27] obtained an experimental correlation $\mathrm{St} = 0.8\mathrm{Ri}^{0.38}$. In buoyant rectangular plumes, a slightly different correlation was obtained as [28]: $\mathrm{St} = 0.55\mathrm{Ri}^{0.45}$. The corresponding puffing frequencies for round and rectangular buoyant plumes are 0.59 and 0.46, respectively, at $\rho_a/\rho = 3$ and $\mathrm{Fr} = 1.5$. Hamins et al. [37] obtained an experimental correlation $\mathrm{St} \sim \mathrm{Fr}^{-0.57}$ for buoyant diffusion flames and $\mathrm{St} \sim \mathrm{Fr}^{-0.38}$ for nonreacting helium plumes. Sato et al. [38] fitted various experimental data of buoyant diffusion flames and arrived at correlations $\mathrm{St} \sim \mathrm{Fr}^{-0.50}$ in the low Froude number range and $\mathrm{St} \sim \mathrm{Fr}^{-0.41}$ in the high Froude number range. In a very different configuration in which the methane-air stream was sandwiched between two annular air streams, Shu et al. [24] obtained an experimental correlation of $\mathrm{St} = 0.43\mathrm{Fr}^{-0.38}$ and a correlation of $\mathrm{St} = 0.56\mathrm{Fr}^{-0.38}$ based on numerical simulations. Whereas exact agreement among these correlations and the present simulation results is impossible because of the variation in the density ratio ρ_a/ρ produced heterogeneously by combustion, all the values of the puffing frequency fall into a narrow range, which suggests that similar mechanisms are behind the puffing. As puffing is associated with the periodic rollup and formation of large vortices near the base, the mechanism behind puffing can be analyzed in detail through the transport equations for vorticity, which after normalization can be expressed in vector form as:

$$\frac{D\boldsymbol{\omega}}{Dt} = \underbrace{(\boldsymbol{\omega}\cdot\nabla)\mathbf{V}}_{\text{vortex stretching}} - \underbrace{\boldsymbol{\omega}(\nabla\cdot\mathbf{V})}_{\text{dilatation term}} + \underbrace{\frac{1}{\rho^2}(\nabla\rho\times\nabla p)}_{\text{baroclinic torque}} + \underbrace{\frac{1}{\rho^2}\frac{\rho_a}{\mathrm{Fr}}(\nabla\rho\times\mathbf{g})}_{\text{gravitational term}} + \underbrace{\nabla\times(\frac{1}{\rho}\nabla\cdot\boldsymbol{\tau})}_{\text{viscous term}}. \tag{2}$$

If the initial vorticities are assumed to be zero, then the vortex stretching and dilatation term will not initiate vorticity. The viscous term is always small compared with other terms. The baroclinic torque and the gravitational term are therefore the dominant mechanisms for vorticity generation at the onset. This can be understood as follows (see Fig. 6): As the fuel stream of higher temperature enters the domain surrounded by the ambient oxidizer stream, a density gradient $\nabla\rho$ is established, which is aligned in the horizontal direction. Since the gravity is aligned in the vertical direction, the gravitational term in Eq. (2) is nonzero, whose magnitude is directly proportional to the density gradient. In the meantime, there is a pressure gradient ∇p in the vertical direction, according to the simplified 1D momentum equation (Bernoulli equation) in the vertical direction:

$$\frac{1}{2}\rho w^2 + p + \rho g_z z = const. \tag{3}$$

or in the differential form:

$$\nabla\left(\frac{1}{2}\rho w^2\right) + \nabla p + \nabla(\rho g_z z) = 0. \tag{4}$$

So even if very near the source the vertical velocity is constant and the density does not change in the vertical direction, the pressure gradient $\nabla p = -\rho_F g_z = \rho_F \neq 0$. Therefore both baroclinic torque and the gravitational term contribute to the initial generation of vorticities, whose strength is mainly dependent on the density gradient and the gravitational force. Moreover,

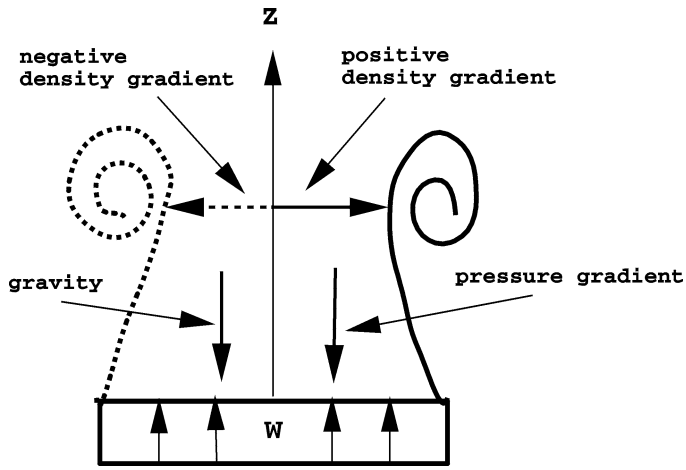

Fig. 6. Mechanisms for vortex generation near the plume source through the baroclinic torque and the gravitational term.

since the density gradient changes sign across the fuel jet centre, vorticities of opposite signs will be generated on different sides of the source, which will lead to the rollup of counter-rotating vortices. These vortices are responsible for the puffing phenomenon described above. As such a phenomenon is caused by an instability which depends on the density distribution and the gravitational force only, it is an *intrinsic buoyancy instability*. Moreover, since no random disturbances are needed to trigger or maintain the instability, it is an *absolute instability* rather than a convective instability as defined by Huerre and Monkewitz [36]. It is self-sustaining as long as there is a buoyancy source. The detailed mechanism for puffing described above can explain the various observations in experiments and simulations. For example, the dependence of the puffing frequency on the ambient pressure observed by Yuan et al. [39] can be attributed to the fact that the ambient pressure changes the pressure gradient ∇p when other conditions are kept the same. Similarly, the correlations between puffing frequency and the Richardson number of Cetegen [27,28] can be justified, because the plume-to-ambient density ratio changes the density gradient $\nabla \rho$ in the baroclinic torque and the gravitational term. However, the correlations of Hamins et al. [37], Sato et al. [38] and Shu et al. [24] may not fully account for the density ratio effects. Indeed, puffing frequencies calculated from these correlations give somehow lower values than from the present DNS results.

Another striking feature of the buoyant reacting plume is the appearance of oscillating energy spectra at high frequencies shown in Fig. 5, which is absent from the spectra of nonreacting flows, e.g., in Fig. 4. It should be noted that these spectra were computed using instantaneous velocity recordings at single locations, without averaging. The oscillations in energy spectra are believed to be mainly an effect of heat release, which takes places at small scales and energizes the flow at certain selected high-frequencies. Nevertheless, the overall trend in the energy decay agrees with the Kolmogorov $-5/3$ power law in the more developed turbulent region downstream ($z = 6$). However, the physical picture of the Kolmogorov turbulence cascade may require modification in reacting flow, since the energy is not transferred monotonically from large scales to successively smaller scales. In fact, volumetric expansion and instabilities induced by combustion are a manifestation of energy "backscatter" from small scales to large scales.

The combustion processes can be better understood by examining the flame structures. Fig. 7 shows a cross-sectional view of the reaction rate ω_T, the mixture fraction dissipation rate χ and the product mass fraction Y_P in the plane $z = 3$ of case Square II. The flame structure is strongly influenced by the large-scale vortex structures induced by buoyancy, and the Biot–Savart instability (see next section) that enhances mixing at the corners. Accordingly, the reaction rate ω_T is large at the four corners of the square flame. Due to vortex extrusion, there are four intensively reactive arms extending from the four corners, forming an outer reaction "ring". As found in [35], the χ-field is characterized by thin sheet-like structures. The high-χ regions promote mixing at the micro-scale level, which in turn would enhance combustion. However, excessively high χ would lead to local flame quenching. Therefore, intense reaction zones in Fig. 7(a) do not always correspond to the high-χ regions in Fig. 7(b). Scatter plots of ω_T against χ (not shown) also reveal that the intense reaction zones and the high scalar dissipation zones are not always coupled in a local and instantaneous sense, due to finite-rate-chemistry effects. Finally, Fig. 7(c) shows that the combustion product has the highest concentration at the four outer arms rather than at the central region, as might be suggested by Fig. 7(a). It again demonstrates that fluid dynamics plays an important role in diffusion flames with finite-rate chemistry.

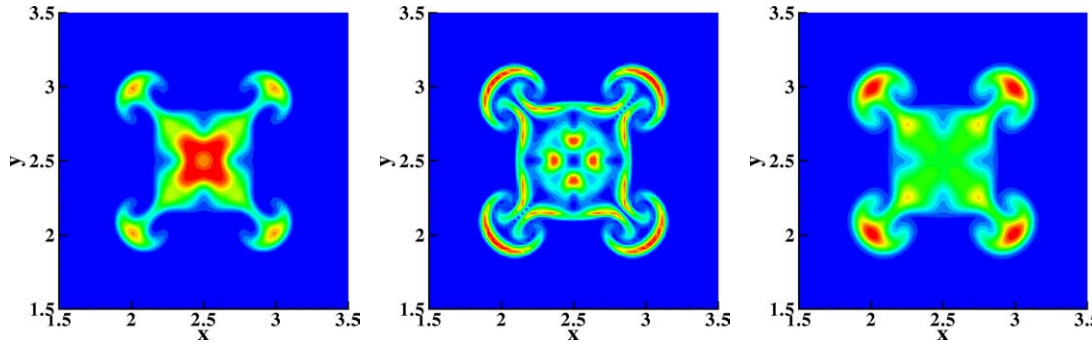

(a) (b) (c)

Fig. 7. Contours of (a) the reaction rate ($0 < \omega_T < 0.016$); (b) the scalar dissipation rate ($0 < \chi < 0.052$); and (c) the product mass fraction ($0 < Y_P < 0.111$) in the plane $z = 3$ at time $t = 24$ of the buoyant diffusion flame from a square source (Square II), showing better mixing and combustion at corners.

4. The Biot–Savart instability

The entrainment rate is a key quantity in buoyant diffusion flames and fires. There have been a wide variety of correlations between the entrainment mass flux and the axial/vertical coordinate z, mostly in the context of fire research. Quintiere and Grove [40] obtained a dependence on $z^{2.5}$ for axisymmetric fires and $z^{1.5}$ for infinite-line fires while Zhou et al. [41] found that data from different experiments would collapse onto a single curve if a normalized entrainment rate was used, which had a dependence on $z^{0.78}$. However, a $z^{5/3}$ power law was found by Zukoski et al. [42] whereas Zukoski [43] modified it to $z^{1.5}$. The large discrepancies in the various correlations were a reflection of the extreme difficulties in measuring the entrainment mass flux and entrainment rate. Different experimental techniques have been used [4,44], which partly explains the large scatter of data found in the literature. Recent non-Boussinesq analysis of buoyant thermal plumes by Rooney and Linden [45] arrived at a $z^{5/3}$ dependence. That study as well as most previous studies assumed an idealized point/line source or an virtual point source with a specified buoyancy flux without a shape, and the results are strictly valid only in the far field. On the other hand, plume development in the far field relies on details of the momentum and buoyancy fluxes at the source and in the near field, which in the case of a reacting plume depends on the detailed combustion processes. Realizing that the large-scale vortical motions are mainly responsible for entrainment in the near field, Cetegen [44] developed a phenomenological entrainment model for axisymmetric fires, which led to a linear dependence of the axial mass flux on the vertical height z. Grinstein and colleagues [16,34,35,46] have systematically investigated the near-field entrainment properties of non-buoyant jets and jet flames, but no parallel studies on buoyant reacting flows were conducted. Recently, Jiang and Luo [14,17] added the buoyancy effects, which led to qualitative and quantitative differences in the flame dynamics and entrainment.

The near-field entrainment properties of the buoyant reacting flow from the rectangular, square and round sources are now compared. Fig. 8 shows the normalized streamwise mass flux and the entrainment rate of buoyant and non-buoyant diffusion flames. The normalized mass flux is defined as

$$\frac{Q_m(z)}{Q_m(0)} = \frac{1}{Q_m(0)} \int_0^{L_y}\int_0^{L_x} \overline{\rho w}\,\mathrm{d}x\,\mathrm{d}y = \frac{1}{Q_m(0)} \int_0^{L_y}\int_0^{L_x} \overline{\rho}(z)\widetilde{w}(z)\,\mathrm{d}x\,\mathrm{d}y, \tag{5}$$

where the overline indicates ensemble average and the tilde refers to the Favre average in a x–y plane. The entrainment rate is defined as $C_e = \mathrm{d}[Q_m(z)/Q_m(0)]/\mathrm{d}z$. Eq. (5) was initially suggested by Ricou and Spalding [47] and has been widely adopted [4,14,17,40]. It should be noted that $\overline{\rho w} = \overline{\rho}(z)\overline{w}(z) + \overline{\rho'(x,y,z)w'(x,y,z)}$. However, in many experiments, the fluctuating part $\overline{\rho'(x,y,z)w'(x,y,z)}$ is ignored. Muñiz [48] estimated that the error due to the neglect of the fluctuating term could be as high as 20%.

It is clear from Fig. 8 that the rectangular buoyant diffusion flame (Rectangular II) entrains more efficiently than both square cases (Square I and II), which in turn are more efficient in entrainment than the round one (Round). The non-reacting but buoyant rectangular case (Rectangular I) entrains poorly compared with all reacting cases. As a comparison, three non-buoyant cases simulated by Grinstein [46] and Grinstein and Kailasanath [34] are also shown. Case pr34 is a non-reacting, rectangular jet of aspect ratio 2 [46]. Case run3 is a non-reacting, square jet while case run5 is a reacting, square jet [34]. As can be seen, buoyant reacting or non-reacting plumes entrain more efficiently than non-buoyant jets. Furthermore, the effects of chemical heat release are different in buoyant and non-buoyant flames. Chemical exothermicity was found to inhibit vortex generation, and relaminarize the flow, leading to a lower entrainment rate (cf. run3 and run5 [34]). Similar phenomena were observed in

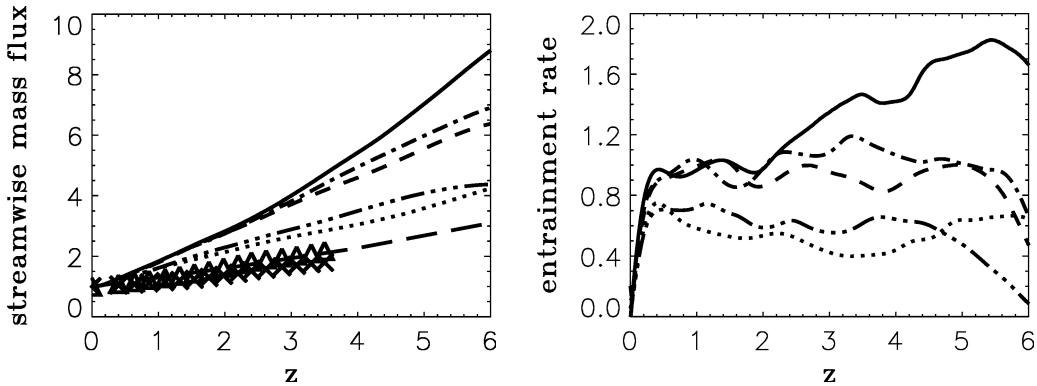

Fig. 8. Comparison of entrainment properties of non-buoyant and buoyant diffusion flames in the near-field (— Rectangular II; ··· Rectangular I; – – – Square I; –·– Square II; –···– Round; ——— Case pr34 [46]; △ run3 [34]; × run5 [34]).

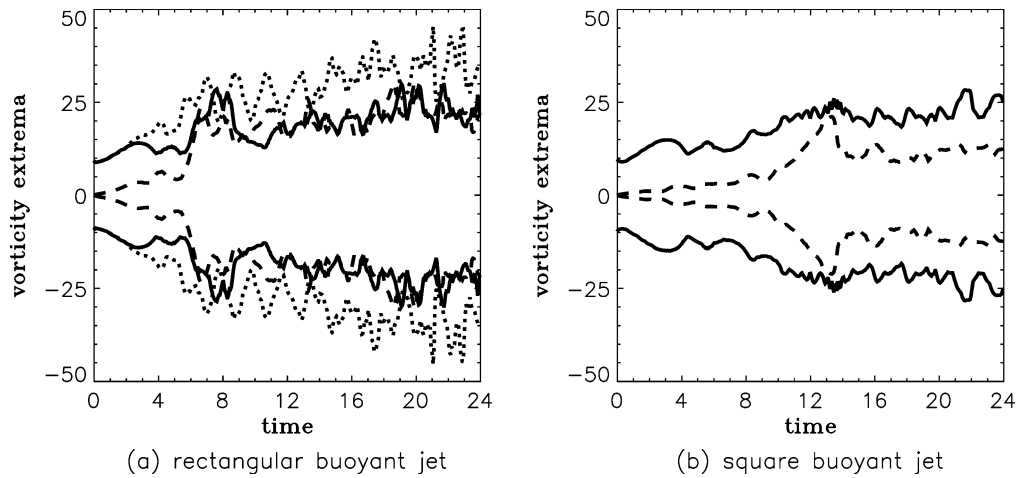

Fig. 9. Comparative history of the vorticity extrema of a rectangular and a square buoyant diffusion flames. (a) Rectangular II; (b) Square I. ((— ω_x; ··· ω_y; – – – ω_z)).

high-speed mixing layers [23], which were attributed to the augmented viscous effects due to large temperature rise associated with combustion. Therefore, there are two competing effects of combustion on entrainment: combustion-induced buoyancy promotes entrainment whereas chemical heat release accompanying combustion reduces entrainment through viscous effects. So the net effect will depend on the relative strength of the two competing factors. In the present simulations, cases Rectangular I and II show an example in which combustion-induced buoyancy effects dominate, so that chemical exothermicity increases the density inhomogeneity and buoyancy level, which results in stronger vortices and consequently better entrainment, which in turn promotes combustion. Therefore, there is a loop of mutual enhancement consisting of fluid dynamics, buoyancy and combustion. On the other hand, cases Square I and II demonstrate that the viscous effects can tip the balance and, as a result, the vorticity level is reduced and entrainment is adversely affected by heat release. Han and Mungal [4] found in their experiments that heat release in reacting jets suppressed entrainment by a factor of 2.5 when compared with nonreacting jets.

The mechanism for the discrepancy in the entrainment rate of non-circular and circular non-buoyant jets was discussed by Gutmark and Grinstein [16]. The Biot–Savart instability [49,50] was identified as a mechanism for vortex-ring deformation, whose rate is measured by the self-induced velocity w_d and is proportional to $C\log(1/\sigma)\vec{b}$, where C is the local azimuthal curvature of a thin inviscid vortex tube, σ the local cross-section of the tube, and $\vec{b}$ the binormal to the plane containing the tube. The Biot–Savart theory predicts that a round, uniform ring would convect with a uniform speed without any change in shape whereas a vortex tube with corners will convect faster at corners than at other locations leading to vortex deformation. This theory can conveniently explain the higher vorticity level and larger entrainment rate in jets/plumes with corners compared with circular ones. However, there has been no clear explanation of the differences between rectangular and square jets/plumes, all of which have corners. In Fig. 9, we show a comparison of the extrema of the three vorticity components in two identical (except for the different base configurations) cases Rectangular II and Square I. As expected, the azimuthal vorticity ω_z in both

cases was initially zero, as there was no azimuthal or any other forcing. The initial vorticity components ω_x and ω_y were the same. However, in Rectangular II, ω_y along the major axis ($L_y = 2L_x$) direction y grew much faster and stayed higher than ω_x along the minor axis (L_x) direction x. It indicates that stronger vortices were formed along the long side of the rectangular flame base than along the short side. As a result, the entrainment and spreading along the major axis was larger than along the minor axis. In comparison, in Square I, ω_x and ω_y remained equal all the time, and their strengths were at a similar level as ω_x in Rectangular II. Therefore, the overall entrainment rate is higher in a rectangular plume than in a square one. The mechanism behind is explained in Section 5.

In order to quantify the effects of flame source configurations on mass entrainment, the following correlation is proposed:

$$\frac{Q_m(z)}{Q_m(0)} = \alpha z^{\beta} + 1. \tag{6}$$

The unknown values of α and β are determined by a least-square fit to the different mass flux curves in Fig. 8. The results for five cases are:

$\alpha = 0.47$, $\beta = 1.08$ Rectangular I,
$\alpha = 0.73$, $\beta = 1.30$ Rectangular II,
$\alpha = 0.65$, $\beta = 1.18$ Square I,
$\alpha = 0.69$, $\beta = 1.22$ Square II,
$\alpha = 0.51$, $\beta = 1.11$ Round I.

As a self-contained comparison, the correlation in Eq. (6) correctly captures the trends in the near-field entrainment in rectangular, square and round/axisymmetric diffusion flames. However, the powers of the z-dependence determined above are obviously different from those reported in [40–43,45]. There are at least two reasons. Firstly, the correlations in the existing literature assume a virtual point source of zero diameter, so that the geometric effects have not been included. Secondly, those correlations are valid for the far-field, whereas the present results are obtained for the near-field. Measurement of the entrainment rate, especially in the near field, is extremely difficult [4,44], so that reliable data for direct comparison is hard to find. One of the few studies involving near-field entrainment measurement was conducted by Han and Mungal [4] using PIV. However, the diffusion flames considered were momentum-driven, which could not be directly compared with the present results. It is worth noting that the measured entrainment rate [4] was not a constant even in the far-field of the reacting jet. All these underline the difficulty of obtaining a "universal" correlation for such highly non-linear phenomena.

Several factors might have affected the entrainment results presented above, although pure numerical errors were strictly controlled in the DNS simulations due to rigorous monitoring and tests. The finite computational box size could affect the

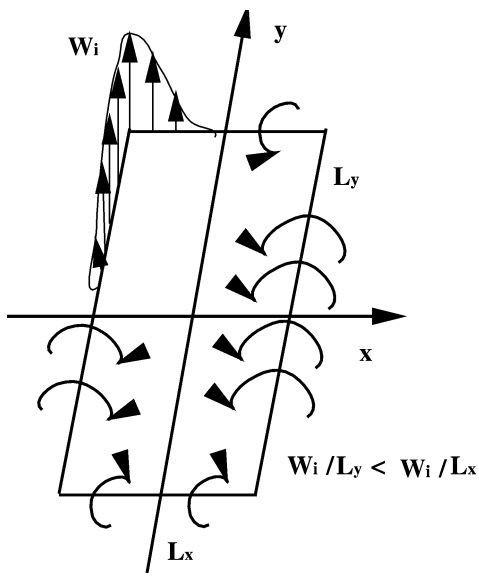

Fig. 10. A mechanism for aspect ratio effects: the self-induced vorticity along the major axis (ω_y) is larger than that along the minor axis (ω_x).

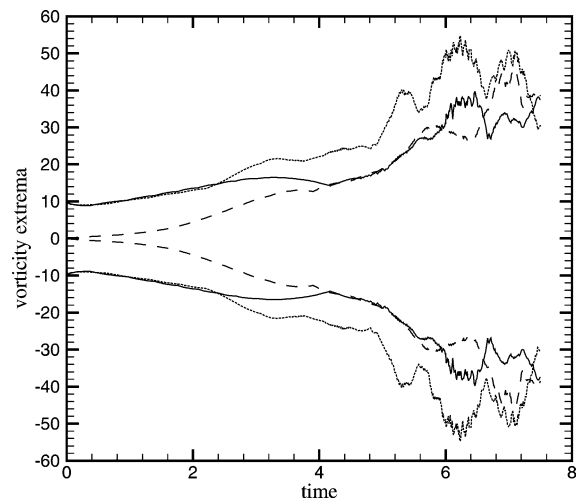

Fig. 11. Vorticity extrema history of the buoyant reacting plume from a rectangular source of aspect ratio 3 (Rectangular III). (— ω_x; $\cdots$ ω_y; $---$ ω_z).

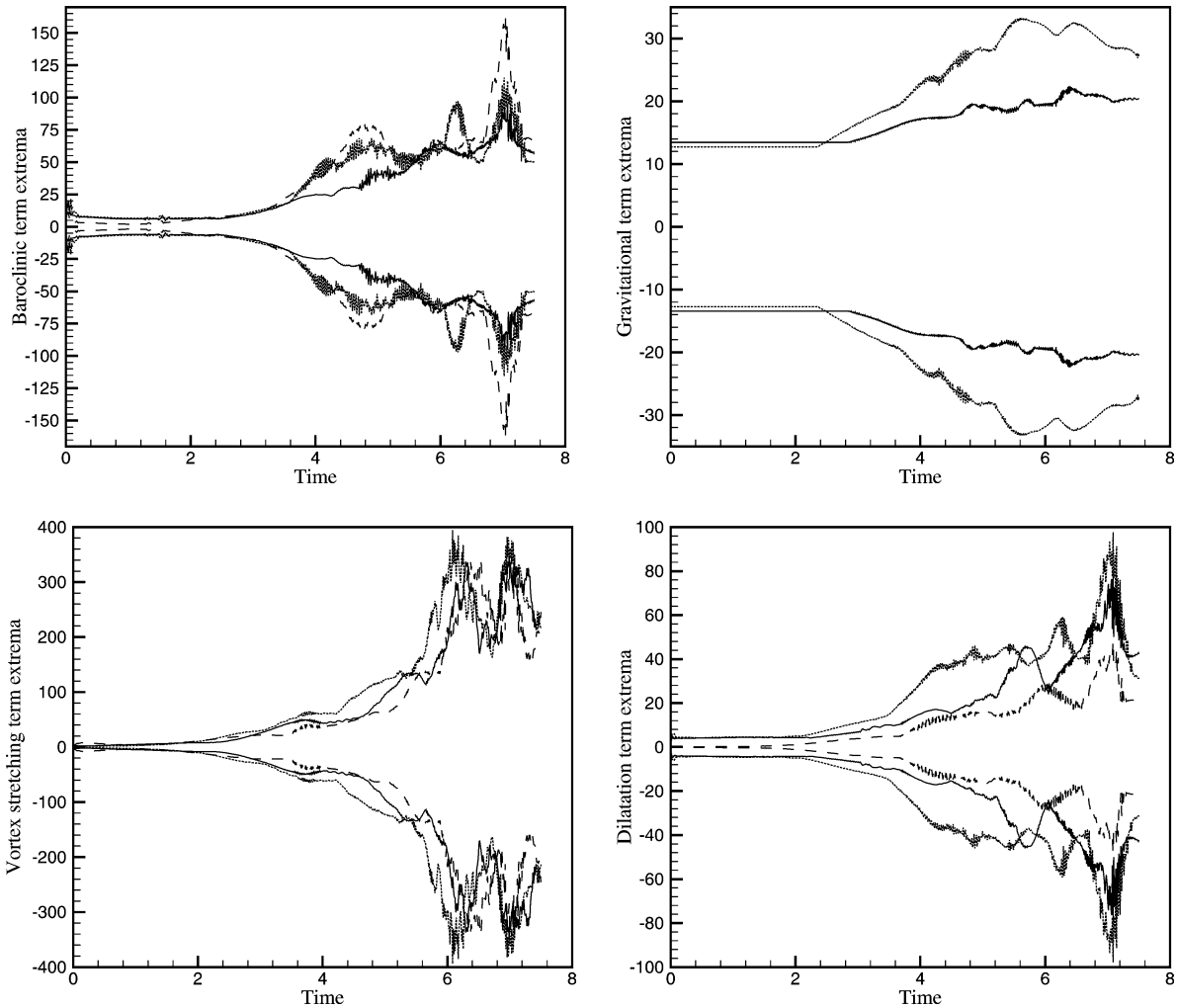

Fig. 12. Time traces of the extrema of the terms in the vorticity transport equations for the three vorticity components of the buoyant reacting plume from a rectangular source of aspect ratio 3 (Rectangular III). (— for ω_x; $\cdots$ for ω_y; $---$ for ω_z).

mass flux calculation if velocity components parallel to boundaries at the lateral boundaries [46] were not zero, as the resulting vorticity would contribute to the vertical mass flux. The lateral boundaries of the present simulations were carefully chosen to be remote enough so that all vorticities and the vertical velocity component were zero at the lateral boundaries (see Figs. 14 and 15). However, the computational box length in the vertical direction was limited by computational resources available, and small errors in the calculation of the vertical mass flux near the outflow boundary could not be avoided. Such errors would be apparent when the entrainment rate (the gradient of mass flux) was calculated, as the sudden drop of C_e at the end of the box might suggest in Fig. 8. Another possibility was statistical errors due to the limited sample data used for calculating the mean quantities. The time duration for averaging was about 12 puffing periods. It was checked that averaging over 10 puffing periods produced almost the same results, so that statistical errors should be negligible.

5. Aspect ratio effects

The aspect ratio effect had been wrongly treated as a mechanism rather than a phenomenon in the existing literature [15]. The present study of reacting flows from different configurations, however, shed new light on the issue. The Biot–Savart instability itself cannot explain why a rectangular jet/plume entrains more efficiently than an equivalent square jet/plume, both of which have corners. But it can be explained as follows. Consider a rectangular plume at the base as a vortex tube "ring", shown in Fig. 10. Biot–Savart instability will induce vertical velocity W_i around the perimeter, whose local magnitude is directly

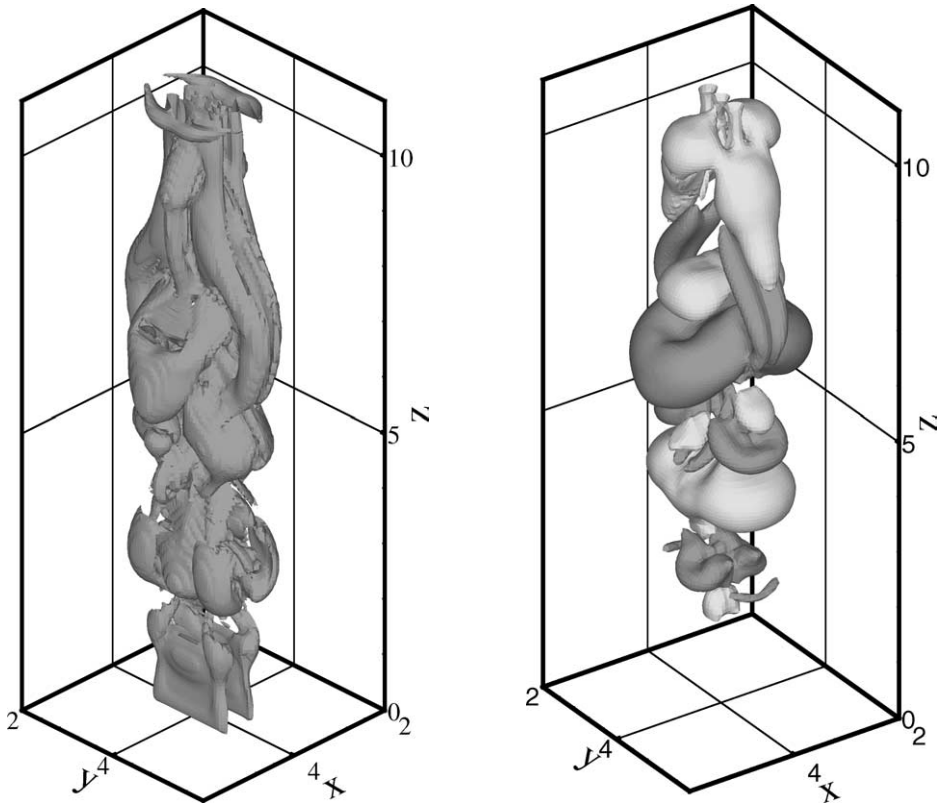

Fig. 13. Representative iso-surfaces of vorticity ω_y (left) and pressure p (right) at $t = 7.5$ of the buoyant reacting plume from a rectangular source of aspect ratio 3 (Rectangular III). The pressure iso-surface plot indicates axis switching at about $z = 6$.

proportional to the local azimuthal curvature. It is observed that from a local point of view, the azimuthal curvature at any 90° corner must be the same, so that W_i of rectangular and square jets at the corners must be the same under identical conditions. At the midpoints along the sides between the corners, $W_i = 0$, since the local curvature is zero. Hence $\omega_x \sim \partial w/\partial y \sim W_{i,\max}/L_y$ and $\omega_y \sim \partial w/\partial x \sim W_{i,\max}/L_x$. Since $L_y > L_x$, we have $\omega_x < \omega_y$, i.e., vorticity along the major axis (y) should be larger than that along the minor axis (x). This is indeed seen in case Rectangular II in Fig. 9. Therefore, entrainment along the major axis will be stronger due to larger ω_y, which tends to make a rectangular jet more square or round. As the trend continues, it may "overshoot" to render the originally minor axis the major axis and vice versa. That is when axis switching occurs. On similar grounds, ω_x and ω_y of the square plume should stay equal to each other, as is indeed the case shown in Fig. 9. However, ω_x and ω_y of Square I are at a similar level as ω_x of the Rectangular II, which means that the rectangular plume should on the whole entrain better due to a larger ω_y.

Furthermore, as L_y increases relative to L_x (i.e., increasing the aspect ratio), the above trends will become stronger, leading to a better overall entrainment in high-aspect-ratio jets/plumes. This is amply demonstrated in case Rectangular III. In Fig. 11, the history of the extrema of the three vorticity components are shown. Although the simulation did not proceed very far due to computational cost consideration, it is seen that by time $t = 6$, the peak ω_y in case Rectangular III is already much larger than that of case Rectangular II over a much longer time period. As expected, ω_y is consistently larger than ω_x, meaning better entrainment along the major axis. The corresponding time traces of the extrema of transport terms for the three vorticity components are shown in Fig. 12. The baroclinic torque and the gravitational term are seen to be the dominant mechanisms for the initial vorticity generation, in agreement with the 1D analysis in Section 3. However, for the present 3D simulation, the dilatation term seems to be important too as a vorticity generation mechanism at the initial stage. At the later stage, the vortex stretching term is the dominant mechanism for vorticity generation for all three components, while the gravitational term becomes almost irrelevant. The baroclinic torque and dilatation term are closely related to the combustion process. The heat release and the accompanying local volume expansion increase the contribution of the dilatation term to vorticity generation. The effect is larger on ω_y than on ω_x, because better entrainment and mixing along the major axis enhances combustion, which in turn has a stronger volume expansion. The same is true of the baroclinic torque, because both the density and pressure

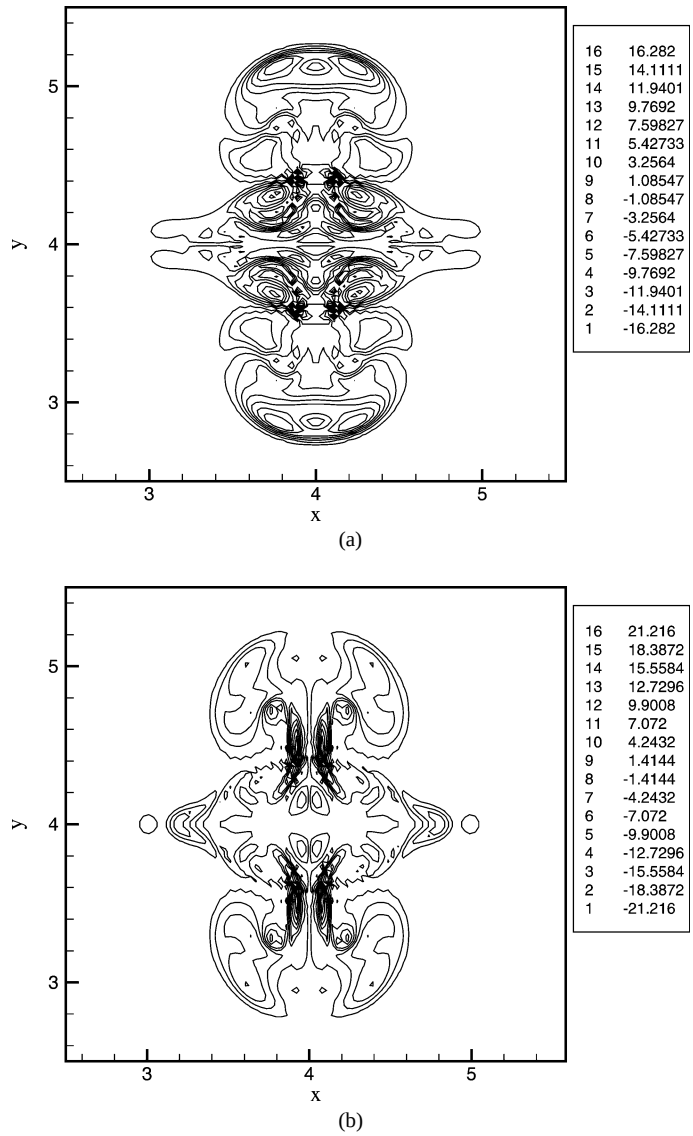

Fig. 14. Contours of the lateral vorticity components (a) ω_x; and (b) ω_y in the plane $z = 5$ at time $t = 7.5$ of the buoyant reacting plume from a rectangular source of aspect ratio 3 (Rectangular III).

gradients ($\nabla\rho$ and ∇p) are steepened by combustion, which is more efficient along the major axis than along the minor axis.

The vortex structures in the high aspect ratio case Rectangular III are now analyzed. Fig. 13 plots representative iso-surfaces of vorticity ω_y and pressure p at $t = 7.5$ of Rectangular III. The pressure iso-surface is a better indication of the vortex structures than any vorticity component [51]. However, the two plots in Fig. 13 indicate very similar vortical structures in the rectangular plume. Close to the base, the vortical structures are mainly aligned along the major axis, due to the initial configuration and the dominance of ω_y. But at about $z = 6$, there is an axis switching as far as the vortex alignment is concerned. Further in the far field, λ-type vortices appear, which are more aligned with the vertical axis z rather than x and y, and are likely to be dominated by ω_z. A x–y plane cut of the vorticity fields (ω_x and ω_y) just below the axis switching is shown in Fig. 14. As expected from the above analysis, vorticity along the major axis ω_y is in general much stronger than that along the minor axis ω_x. In agreement with the Biot–Savart instability, both vorticity components have greater magnitudes at corner regions. The axis switching process is demonstrated in Fig. 15 through the vertical vorticity ω_z fields at two heights. The remarkable fact is that despite the similar ranges of values of ω_z, the axis of the overall vortical pattern changes 90° over a relatively short distance.

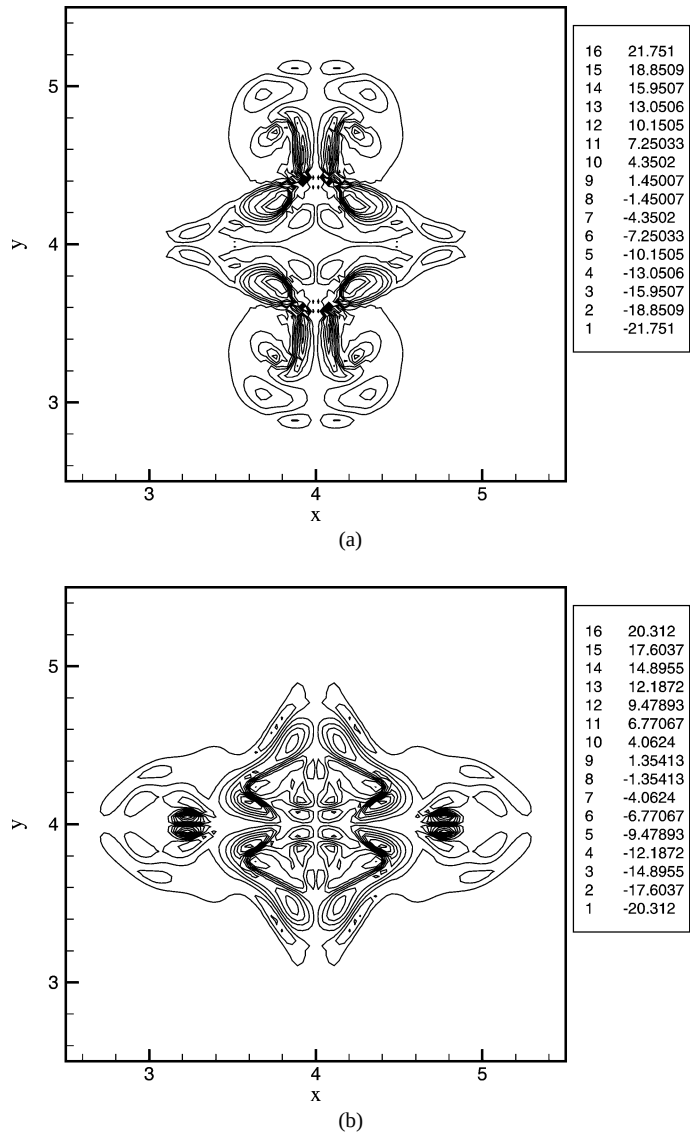

Fig. 15. Contours of the vertical vorticity component ω_z at heights $z = 5$ and 6 at time $t = 7.5$ of the buoyant reacting plume from a rectangular source of aspect ratio 3, showing axis switching (Rectangular III).

Further above $z = 6$, the axes switch again, back to the original orientations. Such phenomena, however, should be anticipated following the above discussion on aspect ratio effects.

6. Discussions and conclusions

Dynamics of buoyant reacting flows from rectangular, square and round sources were well reproduced by a high-order DNS methodology based on first principles for compressible flow and finite-rate Arrhenius chemistry. The salient phenomenon of periodic fluctuations throughout the flow field, called puffing, was observed in all cases, whose oscillation frequency was almost independent of the flow base configurations or heat release, and was in good quantitative agreement with previous experimental data. Unlike most other simulations or experiments, no external disturbances were applied to trigger or sustain the puffing, indicating that puffing in a buoyant reacting flow is a global, absolute instability originated from a local absolute instability near the base. Such an instability depends on the density inhomogeneity (in the gravitational field) only, and is thus an intrinsic instability. The frequency energy spectra of reacting flows were strongly modified by combustion, with the appearance of some

energized modes at high frequencies. The physical picture of the Kolmogorov turbulence cascade should also be modified, since the energy transfer is two-way rather than one-way from large to small scales. Such energy "backscatter" must be represented correctly, in order to model turbulence-combustion interactions.

Combustion had two competing effects on entrainment: combustion-induced buoyancy promoted entrainment whereas chemical heat release accompanying combustion reduced entrainment through viscous effects. So the net effect would depend on the relative strength of the two competing factors. More importantly, entrainment was strongly influenced by the source configurations. The DNS data showed that the entrainment rate in the rectangular buoyant flame was much higher than in the square flame, which in turn had a considerably higher entrainment rate than the round flame. Although such differences were observed before in non-buoyant flows with or without combustion, the discrepancies were much larger in the present buoyant reacting cases. A correlation in the form $Q_m(z)/Q_m(0) = \alpha z^{\beta} + 1$ quantified the geometric effects on entrainment and showed the correct trends.

The source geometry effects on vortex dynamics and entrainment were attributed to the Biot–Savart instability and/or the aspect ratio effects. The Biot–Savart instability, which leads to different vortex deformation rates at different local azimuthal curvatures, can explain why jets/plumes with corners entrain more and spread wider than circular ones. An extension of this argument provided a theoretical explanation for the aspect ratio effects for the first time. It explained why rectangular jets/plumes entrain more than square ones, despite the fact that both configurations have corners. This simple theory was backed by the present DNS data, which showed that the vorticity component along the major axis of a rectangular plume was larger than that along the minor axis, and was also larger than that of a square plume under identical conditions. By increasing the aspect ratio, the vorticity components along both axes were increased, although the vorticity component along the major axis was still consistently larger than that along the minor axis. As a result of different vorticity levels and correspondingly different entrainment rates, rectangular plumes have a tendency to switch major and minor axes, possibly more than once. Such axis switching was observed twice at two vertical locations in the case with aspect ratio 3. Due to the high computational cost required, it was not possible in the present study to obtain more statistical quantities on axis switching and its direct effects on entrainment. Further studies should be conducted to clarify these issues.

The DNS results showed that the structures of the buoyant diffusion flames were strongly influenced by the source configurations. Mixing and combustion were enhanced by the presence of corners in the non-circular source configurations (square and rectangular) as compared with the circular configuration. The complex interactions among instabilities, vortex dynamics and finite-rate chemistry through buoyancy effects led to a rich variety of phenomena, which are not fully accounted for in classical combustion theories. Strong correlations among the small-scale mixing represented by the mixture fraction dissipation rate, chemical reaction rate and the product concentration were not observed at all locations nor at all time instants, due to the different time scales involved. To correctly capture the flame dynamics and resolve flame structures, a RANS approach is unlikely to be successful. A LES has a better chance of success, provided the complex interactions between large and small scales observed in the DNS can be correctly represented by subgrid scale models. The dilemma is that turbulence-combustion interactions at the subgrid-scale level, including the energy "backscatter" described above, are not yet modelled properly on a physical basis. In this context, DNS will continue to serve as a valuable tool for gaining fundamental insight, which will guide us to develop predictive tools and ultimately control algorithms for reacting flows.

Acknowledgement

Special thanks are due to Dr. X. Jiang who generated most of the DNS databases during a project funded by the UK EPSRC under Grant No. GR/L67271/01. Supercomputing resources on the CSAR service from the "UK Turbulence Consortium" (EPSRC Grant No. GR/R64964/01) and the UK "Consortium on Computational Combustion for Engineering Applications" (EPSRC Grant No. GR/R66197/01) are also gratefully acknowledged.

References

[1] S.R. Tieszen, On the fluid mechanics of fires, Annu. Rev. Fluid Mech. 33 (2001) 67–92.
[2] D.L. Urban, M.K. King, NASA's microgravity combustion research program: past and future, Combust. Flame 116 (2) (1999) 319–320.
[3] K.A. Watson, K.M. Lyons, J.M. Donbar, C.D. Carter, Simultaneous Rayleigh imaging and CH-PLIF measurements in a lifted jet diffusion flame, Combust. Flame 123 (2000) 252–265.
[4] D. Han, M.G. Mungal, Direct measurement of entrainment in reacting/nonreacting turbulent jets, Combust. Flame 124 (2001) 370–386.
[5] S.R. Tieszen, T.J. O'hern, R.W. Schefer, T.K. Blanchat, Experimental study of the flow field in and around a one-meter diameter methane fire, Combust. Flame 129 (2002) 378–391.
[6] G. Cox, Turbulent closure and the modelling of fire using computational fluid dynamics, Philos. Trans. Roy. Soc. Ser. A 356 (1748) (1998) 2835–2854.

[7] K.B. McGrattan, H.R. Baum, R.G. Rehm, Large eddy simulation of smoke movement, Fire Safety J. 30 (1998) 161–1178.
[8] X. Zhou, K.H. Luo, J.J.R. Williams, Dynamic behaviour in reacting plumes, Proc. Combust. Inst. 28 (2000) 2859–2865.
[9] X. Zhou, K.H. Luo, J.J.R. Williams, Numerical studies on vortex structures in the near-field of oscillating diffusion flames, Heat Mass Transfer 37 (2001) 101–110.
[10] X. Zhou, K.H. Luo, J.J.R. Williams, Vortex dynamics in spatio-temporal development of reacting plumes, Combust. Flame 129 (2002) 11–29.
[11] L. Vervisch, T. Poinsot, Direct numerical simulation of non-premixed turbulent combustion, Annu. Rev. Fluid Mech. 30 (1998) 655–691.
[12] K.H. Luo, Direct and large eddy simulation of turbulence–combustion interactions, in: R.T. Edwards (Ed.), Modern Simulation Strategies for Turbulent Flow, Edwards, Philadelphia, 2001, pp. 263–293, Chapter 14.
[13] X. Jiang, K.H. Luo, Combustion-induced buoyancy effects of an axisymmetric reactive plume, Proc. Combust. Inst. 28 (2000) 1989–1995.
[14] X. Jiang, K.H. Luo, Direct numerical simulation of transitional non-circular buoyant reactive jets, Theoret. Comput. Fluid Dynamics 15 (2001) 183–198.
[15] K.H. Luo, X. Jiang, Passive control of flow entrainment in buoyant reacting jets, in: I.P. Castro, P.E. Hancock, T.G. Thomas (Eds.), Advances in Turbulence IX, Proc. Ninth European Turbulence Conference, Southampton, UK, 2–5 July, 2002, pp. 569–572.
[16] E.J. Gutmark, F.F. Grinstein, Flow control with noncircular jets, Annu. Rev. Fluid Mech. 31 (1999) 239–272.
[17] X. Jiang, K.H. Luo, Mixing and entrainment of transitional noncircular buoyant reactive plumes, Flow, Turbulence and Combustion 67 (1) (2001) 57–79.
[18] K.H. Luo, X. Jiang, Direct numerical simulation of reacting corner plumes, in: I.P. Castro, P.E. Hancock, T.G. Thomas (Eds.), Advances in Turbulence IX, Proc. Ninth European Turbulence Conference, Southampton, UK, 2–5 July, 2002, pp. 351–354.
[19] P. Moin, K. Mahesh, Direct numerical simulation: a tool in turbulence research, Annu. Rev. Fluid Mech. 30 (1998) 539–578.
[20] B. Rembold, N.A. Adams, L. Kleiser, Direct numerical simulation of a transitional rectangular jet, Int. J. Heat Fluid Flow 23 (5) (2002) 547–553.
[21] N. Docquier, S. Candel, Combustion control and sensors: a review, Prog. Energy Combust. Sci. 28 (2) (2002) 107–150.
[22] M. Mettenleiter, F. Vuillot, S. Candel, Numerical simulation of adaptive control: application to unstable solid rocket motors, AIAA J. 40 (5) (2002) 860–868.
[23] K.H. Luo, Combustion effects on turbulence in a partially premixed supersonic diffusion flame, Combust. Flame 119 (4) (1999) 417–435.
[24] Z. Shu, S.K. Aggarwal, V.R. Katta, I.K. Puri, Flame-vortex dynamics in an inverse partially premixed combustor: the Froude number effects, Combust. Flame 111 (4) (1997) 276–295.
[25] T.J. Poinsot, S.K. Lele, Boundary conditions for direct simulations of compressible viscous flows, J. Comput. Phys. 101 (1992) 104–129.
[26] B.M. Cetegen, T.A. Ahmed, Experiments on the periodic instability of buoyant plumes and pool fires, Combust. Flame 93 (1993) 157–184.
[27] B.M. Cetegen, Behavior of naturally unstable and periodically forced axisymmetric buoyant plumes of helium and helium–air mixtures, Phys. Fluids 9 (12) (1997) 3742–3752.
[28] B.M. Cetegen, Y. Dong, M.C. Soteriou, Experiments on stability and oscillatory behavior of planar buoyant plumes, Phys. Fluids 10 (1998) 1658–1665.
[29] A.F. Ghoniem, I. Lakkis, M. Soteriou, Numerical simulation of the dynamics of large fire plumes and the phenomenon of puffing, Proc. Combust. Inst. 26 (1996) 1531–1539.
[30] J. Buckmaster, N. Peters, The infinite candle and its stability – a paradigm for flickering diffusion flame, Proc. Combust. Inst. 21 (1986) 1829–1836.
[31] A. Lingens, M. Reeker, M. Schreiber, Instability of buoyant diffusion flames, Exp. Fluids 20 (1996) 241–248.
[32] T. Maxworthy, The flickering candle: transition to a global oscillation in a thermal plume, J. Fluid Mech. 390 (1999) 297–323.
[33] V.R. Katta, L.P. Goss, W.M. Roquemore, Numerical investigations of transitional H_2/N_2 jet diffusion flames, AIAA J. 32 (1) (1994) 84–94.
[34] F.F. Grinstein, K. Kailasanath, Three-dimensional numerical simulations of unsteady reactive square jets, Combust. Flame 100 (1995) 2–10.
[35] F.F. Grinstein, K. Kailasanath, Exothermicity and relaminarization effects in unsteady reactive square jets, Combust. Sci. Technol. 114 (1996) 291–312.
[36] P. Huerre, P.A. Monkewitz, Local and global instabilities in spatially developing flows, Annu. Rev. Fluid Mech. 22 (1990) 473–537.
[37] A. Hamins, J.C. Yang, T. Kashiwagi, An experimental investigation of the pulsation frequency of flames, Proc. Combust. Inst. 24 (1992) 1695–1702.
[38] H. Sato, K. Amagai, M. Arai, Diffusion flames and their flickering motions related with Froude numbers under various gravity levels, Combust. Flame 123 (2000) 107–118.
[39] T. Yuan, D. Durox, E. Villermaux, An analogue study for flame flickering, Exp. Fluids 17 (1994) 337–349.
[40] J.G. Quintiere, B.S. Grove, A unified analysis for fire plumes, Proc. Combust. Inst. 27 (1998) 2757–2766.
[41] X.C. Zhou, J.P. Gore, H.R. Baum, Measurements and predictions of air entrainment rates of pool fires, Proc. Combust. Inst. 26 (1996) 1453–1459.
[42] E.E. Zukoski, T. Kubota, B.M. Cetegen, Entrainment in fire plumes, Fire Safety J. 3 (1980) 107–121.
[43] E.E. Zukoski, Properties of fire plumes, in: G. Cox (Ed.), Combustion Fundamentals of Fire, Academic Press, San Diego, 1995, pp. 101–219.
[44] B.M. Cetegen, A phenomenological model of near-field fire entrainment, Fire Safety J. 31 (1998) 299–312.
[45] G.G. Rooney, P.F. Linden, Similarity considerations for non-Boussinesq plumes in an unstratified environment, J. Fluid Mech. 318 (1996) 237–250.
[46] F.F. Grinstein, Vortex dynamics and entrainment in rectangular free jets, J. Fluid Mech. 437 (2001) 69–101.

[47] F.P. Ricou, D.B. Spalding, Measurements of entrainment by axisymmetrical turbulent jets, J. Fluid Mech. 8 (1961) 21–32.
[48] L. Muñiz, Particle image velocimetry studies of turbulent non-premixed flames, Ph.D. Thesis, Stanford University, California, 2000.
[49] G.K. Batchelor, An Introduction to Fluid Dynamics, Cambridge University Press, Cambridge, 1967.
[50] P.G. Saffman, Vortex Dynamics, Cambridge University Press, Cambridge, 1992.
[51] N.D. Sandham, W.C. Reynolds, Three-dimensional simulations of large eddies in the compressible mixing layer, J. Fluid Mech. 224 (1991) 133–158.